


# Joint inversion of daily and long-period geomagnetic transfer functions reveals lateral variations in mantle water content

**Journal Article****Author(s):**

Munch, Federico D.; Grayver, Alexander V.; Guzavina, Martina; Kuvshinov, Alexey; [Khan, Amir](#) 

**Publication date:**

2020-05-28

**Permanent link:**

<https://doi.org/10.3929/ethz-b-000410771>

**Rights / license:**

[In Copyright - Non-Commercial Use Permitted](#)

**Originally published in:**

Geophysical Research Letters 47(10), <https://doi.org/10.1029/2020gl087222>

**Funding acknowledgement:**

159907 - The thermo-chemical structure of Earth's mantle from joint analysis of seismic and electromagnetic sounding data and thermodynamic modeling (SNF)



# Joint inversion of daily and long-period geomagnetic transfer functions reveals lateral variations in mantle water content

F. D. Munch<sup>1</sup>, A. V. Grayver<sup>1</sup>, M. Guzavina<sup>1</sup>, A. V. Kuvshinov<sup>1</sup>, A. Khan<sup>1,2</sup>

<sup>1</sup>Institute of Geophysics, ETH Zurich, Switzerland

<sup>2</sup>Institute of Theoretical Physics, University of Zurich, Switzerland.

## Key Points:

- Joint inversion of daily and long-period geomagnetic variations results in better resolved mantle conductivity structure
- Incorporation of seismic constraints helps isolate mantle water content
- We find a relatively dry mantle beneath Europe and a water-enriched transition zone underneath North America and northern Asia

---

Corresponding author: Federico D. Munch, [fmunch@seismo.berkeley.edu](mailto:fmunch@seismo.berkeley.edu)

Present address: Berkeley Seismological Laboratory, University of California, Berkeley, CA 94720, USA.

This article has been accepted for publication and undergone full peer review but has not been through the copyediting, typesetting, pagination and proofreading process which may lead to differences between this version and the Version of Record. Please cite this article as doi: 10.1029/2020GL088133

## Abstract

We present a novel approach to investigate variations in upper mantle and transition zone (MTZ) water content based on the joint analysis of electromagnetic (EM) signals originating in the ionosphere and magnetosphere. We invert EM signals (period range 6 hours–85 days) to probe the electrical conductivity structure underneath 20 geomagnetic observatories, accounting for the complex spatial structure of the ionospheric and magnetospheric sources. The joint inversion of EM data for the daily and long-period bands lead to significantly improved resolution in the upper mantle and MTZ. The conductivity profiles reveal significant lateral variability, which we interpret in terms of mantle water content by coupling electrical conductivity with constraints on mantle thermochemical structure derived from the analysis of seismic data. Our results suggest the existence of a relatively dry MTZ beneath Europe and a water-enriched MTZ underneath North America and northern Asia.

## Plain Language Summary

The amount of water (hydrogen) trapped in the Earth's interior has a strong effect on the evolution and dynamics of the planet, which ultimately controls the occurrence of earthquakes and volcanic eruptions. However, the distribution of water inside the Earth is yet not well-understood. Deep electromagnetic induction techniques make use of changes in the Earth's magnetic field to detect variations in electrical conductivity inside the planet. Electrical conductivity is a characteristic of a rock that varies with temperature and the amount of water in its interior. Here, we present a methodology that combines different deep electromagnetic induction techniques to estimate the amount of water in different regions of Earth's mantle. Our analysis suggests the presence of small amounts of water in the mantle underneath Europe, whereas larger amounts are found beneath North America and northern Asia. These findings help revealing the complexity of the water cycle and can potentially be used to benchmark predictions from studies that simulate mantle dynamics.

## 1 Introduction

Constraining the water (hydrogen) distribution in Earth's interior is important for understanding its evolution and dynamics since water has a profound effect on rheological properties and melting relationships [e.g., *Hirschmann, 2006; Karato, 2011*]. High-pressure mineral-physics studies have reported that mantle transition zone (MTZ) minerals can store large amounts of water (~1–3 wt%), whereas much smaller amounts (~0.1–0.2 wt%) can be stored in upper mantle minerals

43 [e.g., *Hirschmann et al.*, 2005; *Bolfan-Casanova*, 2005]. Supporting evidence for a relatively dry  
44 (~0.02 wt%) upper mantle and a hydrous (~1 wt%) MTZ has been provided by the analysis of mantle  
45 xenoliths [e.g., *Peslier et al.*, 2010; *Peslier and Bizimis*, 2015] and ringwoodite inclusions found in  
46 a natural diamond that truly originated in the MTZ [*Pearson et al.*, 2014], respectively. However,  
47 the present distribution of water in the Earth's interior and the mechanisms for water exchange  
48 between different mantle reservoirs remain uncertain [e.g., *Ohtani et al.*, 2004; *Hirschmann*, 2006;  
49 *Bolfan-Casanova et al.*, 2006].

50 As electrical conductivity is a transport property that is highly sensitive to mantle temperature  
51 and the presence of water and melt [e.g., *Karato*, 2011; *Katsura and Yoshino*, 2015; *Khan*, 2016],  
52 deep electromagnetic (EM) sounding techniques play a fundamental role in mapping the distribution  
53 of water in the mantle by imaging variations in electrical conductivity [e.g., *Koyama et al.*, 2006;  
54 *Kelbert et al.*, 2009; *Shimizu et al.*, 2010; *Semenov and Kuvshinov*, 2012; *Koyama et al.*, 2014; *Sun*  
55 *et al.*, 2015]. These techniques rely on the fact that primary magnetic fields (e.g., those that originate  
56 in the magnetosphere) penetrate into the deep Earth and induce secondary signals by virtue of EM  
57 induction. EM variations in the daily band (4–24 hours) are mainly dominated by the ionospheric  
58 current system, while variations with periods longer than one day are generated by magnetospheric  
59 currents [e.g., *Finlay et al.*, 2017]. As penetration depth depends on frequency, analyzing these  
60 signals in as wide a range of periods as possible allows us to sense electrical conductivity variations  
61 in the widest depth range possible [e.g., *Püthe et al.*, 2015a]. However, EM sounding studies often  
62 rely on single-source data analysis facing the problem of limited depth resolution due to a limited  
63 frequency range imposed by various source morphologies [cf., *Kuvshinov*, 2008].

64 Only a few studies have attempted to combine EM responses from different sources. For  
65 instance, *Egbert and Booker* [1992] and *Bahr et al.* [1993] combined signals from magnetospheric  
66 and ionospheric origin recorded at geomagnetic observatories to obtain regional conductivity models  
67 of the mantle underneath North America and Europe, respectively. These studies, however, invoked  
68 simplistic source assumptions, which is likely to increase the chance of introducing source related  
69 model biases. Alternatively, *Olsen* [1998] accounted for a more complex source geometry (in the  
70 period range 3–720 hr) by incorporating estimates of horizontal gradients of the horizontal magnetic  
71 field. Given that direct measurement of these gradients on a single site is challenging in practice,  
72 the author estimated gradients from horizontal magnetic field components measured at an array of  
73 nearby observatories, which is limited to regions with a dense network of geomagnetic observatories  
74 (e.g., Europe). More recently, *Grayver et al.* [2017] jointly inverted the magnetospheric global

75 response and ocean tidal signals from satellite magnetic field measurements, yielding a consistent  
76 global conductivity model of the oceanic upper mantle and transition zone.

77 Here, we perform inversions of daily (6–24 hours) and long-period (3–85 days) local responses  
78 recorded at a series of geomagnetic observatories to infer lateral variations in upper mantle and MTZ  
79 conductivity structure and water content. To isolate the influence of water on electrical conductivity  
80 from thermal effects, we follow *Khan* [2016] and combine phase equilibrium calculations, laboratory-  
81 measured electrical conductivity of mantle minerals, and estimates of mantle temperature and major  
82 element chemistry derived from the analysis of short- and long-period seismic data using the results  
83 of *Munch et al.* [2020, in press].

## 84 2 Methods

### 85 2.1 Multi-source EM global-to-local transfer functions

86 Signals due to the magnetospheric currents dominate natural geomagnetic variations at periods  
87 longer than one day [cf., *Finlay et al.*, 2017; *Olsen and Stolle*, 2017]. The source of these signals is  
88 often described via a single – first zonal – spherical harmonic, leading to the widely-used local C-  
89 response [*Banks*, 1969]. This transfer function (TF) relates vertical and horizontal components of the  
90 magnetic variations at an observational site. However, it is known that the magnetospheric source has  
91 a more complex structure, especially during the main phase of geomagnetic storms [e.g., *Daglis and*  
92 *Kozyra*, 2002; *Olsen and Kuvshinov*, 2004; *Balasis and Egbert*, 2006], thus potentially introducing  
93 errors in the estimated responses, resulting in biases in the retrieved conductivity structure [e.g.,  
94 *Püthe et al.*, 2015b]. Furthermore, geomagnetic field variations in the period range between a few  
95 hours and one day are dominated by the ionospheric current systems which are characterized by a  
96 more complex morphology [e.g., *Yamazaki and Maute*, 2017]. This complexity invalidates simplistic  
97 source models that would allow the use of a TF similar to the C-response. To account for complex  
98 ionospheric and magnetospheric sources, we resort here to an alternative set of global-to-local  
99 transfer functions,  $T_n^m(\mathbf{r}_a, \omega)$ , that relate the vertical component of the magnetic field  $Z(\mathbf{r}_a, \omega)$  at an  
100 observation site  $\mathbf{r}_a = (a, \theta, \varphi)$  to a set of global spherical harmonic expansion (SHE) coefficients,  
101  $\varepsilon_n^m(\omega)$ , that describe the source structure [*Püthe et al.*, 2015b]

$$Z(\mathbf{r}_a, \omega) = \sum_{n=1}^{N_\varepsilon} \sum_{m=-n}^n \varepsilon_n^m(\omega) T_n^m(\mathbf{r}_a, \omega), \quad (1)$$

102 where  $N_\varepsilon$  is the maximum (cut-off) degree for the external SHE coefficients,  $\omega$  is the angular  
103 frequency,  $a$  denotes the Earth's mean radius,  $\theta$  is the colatitude, and  $\varphi$  is the longitude.

104 The estimation of global-to-local TFs is a two step procedure: (i) external SHE coefficients  
 105 describing the source are determined from horizontal components of the magnetic field measured  
 106 at a global network of geomagnetic observatories assuming an a priori three-dimensional (3-D)  
 107 Earth model, which consists of a mantle with a one-dimensional (1-D) conductivity distribution  
 108 overlaid by a laterally-varying surface conductance layer; the latter approximates the nonuniform  
 109 distribution of oceans and continents (see Appendix A for details on estimating “magnetospheric”  
 110 source coefficients); and (ii) TFs are estimated by relating the vertical component of the magnetic  
 111 field measured at every site of interest with the source coefficients determined in the previous step.  
 112 The data for estimating “magnetospheric” TFs consist of hourly mean values of geomagnetic field  
 113 variations measured at 132 mid-latitude (geomagnetic latitudes between  $\pm 6^\circ$  and  $\pm 56^\circ$ ) permanent  
 114 geomagnetic observatories (see Figure S1) for the years 1998–2018 retrieved from the British  
 115 Geological Survey (BGS) database [Macmillan and Olsen, 2013]. After removal of the main field  
 116 and its secular variations using the CHAOS model [Olsen et al., 2006], source coefficients and  
 117 global-to-local transfer functions for the long-period band (3–85 days) were determined following  
 118 the procedures described in Püthe et al. [2015b], which includes section-averaging [e.g., Olsen, 1998]  
 119 and Huber-weighted robust least-squares methods [e.g., Aster et al., 2005]. As for global-to-local  
 120 TFs in the daily band (24, 12, 8, and 6 hours), we used those estimated by Guzavina et al. [2019]  
 121 from the BGS database. Geographic and geomagnetic coordinate systems were used for estimating  
 122 “daily” and “long-period” TFs, respectively.

## 123 2.2 Probabilistic inversion

124 We employed the probabilistic approach of Tarantola and Valette [1982] and the Metropolis  
 125 algorithm [e.g., Metropolis et al., 1953; Hastings, 1970] to determine the conductivity structure  
 126 underneath each station from the estimated global-to-local TFs. Building on previous experience  
 127 [Munch et al., 2018], we reduced the burn-in stage of the Metropolis algorithm by using a global  
 128 optimization technique [Covariance Matrix Adaptation Evolution Strategy; Hansen and Ostermeier,  
 129 2001] to obtain a good initial model  $\mathbf{m}_0$  for every inversion. The solution of the non-linear inverse  
 130 problem is then given in terms of the posterior probability distribution

$$131 \gamma(\mathbf{m}|\mathbf{d}) \propto \exp\left[-\frac{\phi(\mathbf{m}, \mathbf{d})}{2}\right] \exp\left[-\frac{\beta}{p_m} \sum_{i=1}^M |\nabla \mathbf{m}_i|^{p_m}\right], \quad (2)$$

132 where  $\mathbf{d}$  denotes observed data and  $\mathbf{m} = [\lambda(\sigma_1) \cdots \lambda(\sigma_N)]$  represents the unknown conductivity  
 133 structure, with  $\lambda(\cdot)$  being a log-based transformation ensuring positivity of the argument. The  
 134 subsurface was parametrized in terms of 25 layers ranging in thickness from 50 km in the upper  
 mantle and MTZ to 400 km at the core-mantle boundary with a fixed core conductivity ( $\sigma = 10^5$

S/m). The regularization parameter  $\beta$  was determined by means of an L-curve analysis [Hansen, 1999] performed on the models  $\mathbf{m}_0$  and the scalar  $p_m$  was set to 1.5 which provides a good balance between sharp conductivity contrasts and smooth models [Grayver and Kuvshinov, 2016]. The data misfit term is given by

$$\phi(\mathbf{m}, \mathbf{d}) = \sum_{k \in \mathcal{M}} \left( \frac{1}{N_k} \sum_{i=1}^{N_k} |w_i^k (f_i^k(\mathbf{m}) - d_i^k)|^2 \right), \quad (3)$$

where  $\mathcal{M}$  denote the EM methods in the daily and long-period bands and  $w^k$ ,  $f^k(\mathbf{m})$ , and  $d^k$  are corresponding data weights (reciprocal of uncertainties), forward operator, and observed data, respectively. As discussed by Grayver *et al.* [2017], normalizing with the number of actual measurements ( $N_k$ ) is an important aspect that helps balance the contribution of each EM technique.

### 2.3 Inference of water content from retrieved conductivity profiles

We interpreted the obtained conductivity profiles in terms of upper mantle and transition zone water content by comparing the retrieved models with laboratory-based conductivity profiles computed using the approach of Khan [2016]. To isolate the influence of water on electrical conductivity from thermal effects, we constrained mantle temperature and major element chemistry underneath each geomagnetic observatory by incorporating into the inversion probability density functions independently derived from the inversion of short- (P-to-s receiver functions) and long-period (Rayleigh wave phase velocities) seismic data from a nearby seismic station [Munch *et al.*, 2020, in press]. Mantle composition was parameterized in terms of a single variable that represents the amount of basalt in a basalt-harzburgite mixture, with the composition of basalt and harzburgite end-members described using the CFMASNa chemical model system comprising the oxides CaO-MgO-FeO-Al<sub>2</sub>O<sub>3</sub>-SiO<sub>2</sub>-Na<sub>2</sub>O. Mantle temperature was described in terms of an adiabat defined by the mantle potential temperature  $T_p$ , which represents the temperature that the mantle would have at the surface, if it ascended along an adiabat without undergoing melting [McKenzie and Bickle, 1988].

The laboratory-based conductivity profiles were computed from mineral phase equilibrium calculations and experimental measurements of mantle mineral conductivities. We employed the Gibbs free-energy minimization strategy of Connolly [2009] and the self-consistent thermodynamic formulation of Stixrude and Lithgow-Bertelloni [2005] with parameters given by Stixrude and Lithgow-Bertelloni [2011] to predict stable mineralogy (mineral modes) as a function of pressure, temperature, and composition. Several independent measurements of the electrical conductivity for major upper

164 mantle and MTZ minerals exist. To minimize subjectivity, we here considered two databases built  
 165 on the measurements of (i) Yoshino, Katsura, and coworkers (referred to as YK) and (ii) Karato, Dai,  
 166 and coworkers (referred to as KD). Table S2 provides the list of data sources used to build the YK  
 167 and KD databases. The laboratory-measured databases account for the effect of water content on the  
 168 following hydrous minerals: olivine, orthopyroxene, clinopyroxene, wadsleyite, ringwoodite, and  
 169 garnet (only KD database). Building on previous experience [e.g., *Khan*, 2016], we parameterized  
 170 the water content of the mantle in terms of the water contents in olivine (upper mantle) and wadsleyite  
 171 (transition zone). Water contents in orthopyroxene, clinopyroxene, and ringwoodite were estimated  
 172 using the water partition coefficients based on measurements from *Inoue et al.* [2010] and *Ferot and*  
 173 *Bolfan-Casanova* [2012]. Water content in garnet (only relevant for KD database) was estimated  
 174 using the water partition coefficients derived by *Mookherjee and Karato* [2010].

### 175 3 Results

#### 176 3.1 Long-period transfer functions

177 As discussed above, we estimated global-to-local transfer functions in the period range 3–85  
 178 days from 21 years (1998–2018) of ground-based geomantic observatory data. In order to better  
 179 account for the complexity of the source, magnetospheric time series were parameterized in terms  
 180 of 13 SHE coefficients ( $\varepsilon_1^0, \varepsilon_1^1, \varepsilon_1^{-1}, \varepsilon_2^0, \varepsilon_2^1, \varepsilon_2^{-1}, \varepsilon_2^2, \varepsilon_2^{-2}, \varepsilon_3^2, \varepsilon_3^{-2}, \varepsilon_4^0, \varepsilon_4^1$ , and  $\varepsilon_4^{-1}$ ). The choice of source  
 181 coefficients aims at maximizing the coefficient of determination (i.e., measure of how well a proposed  
 182 source geometry predicts the observed time series; see Figure S2), while minimizing the number  
 183 of source terms that limits the maximum period for which multi-variate transfer functions can be  
 184 estimated [*Püthe and Kuvshinov*, 2014] and that may result in over-fitting. All source terms were  
 185 used to estimate long-period global-to-local transfer functions  $T_n^m$ , but only the dominant source  
 186 term  $T_1^0$  was considered in the inversion to retrieve the conductivity structure underneath each station  
 187 because this TF is most sensitive to the radial structure of the Earth [*Kuvshinov*, 2008]. In the daily  
 188 band, we also considered only TFs corresponding to dominant source terms, namely,  $T_p^{p+1}$  at periods  
 189  $24/p$  hr ( $p = 1 - 4$ ). As discussed in Section 2.1, the estimation of source coefficients requires  
 190 the assumption of a mantle 1-D conductivity profile to separate the external (inducing) from the  
 191 internal (induced) contributions in the measured geomagnetic variations. We find that differences  
 192 in the long-period TFs introduced by the choice of the mantle conductivity profile are within data  
 193 uncertainties (see Figure S3).



194 Figure 1a depicts estimated long-period responses  $T_1^0$ , uncertainties, and squared coherencies  
 195 ( $\text{coh}^2$ ) for four geomagnetic observatories: Boulder (BOU, USA), Niemegk (NGK, Germany), Belsk  
 196 (BEL, Poland), and Irkutsk (IRT, Russia). For comparison, transfer functions  $\hat{T}_1^0$  estimated assuming  
 197 that the source is described by the first zonal spherical harmonic are also shown. In this case,  
 198 the TFs were derived from the local C-response  $C(\mathbf{r}_a, \omega)$  – estimated using the Z/H method of  
 199 *Banks* [1969] – as  $\hat{T}_1^0(\mathbf{r}_a, \omega) = \frac{3C(\mathbf{r}_a, \omega)}{C(\mathbf{r}_a, \omega) + a} \cos \theta$ . In agreement with previous studies [*Püthe et al.*,  
 200 2015b], we find that the incorporation of additional source terms increases the squared coherency,  
 201 especially at periods  $< 10$  days and geomagnetic latitudes  $> 40^\circ$ , thus decreasing the potential bias of  
 202 the responses that could result from correlated noise and spatial aliasing [*Olsen*, 1998]. Figure 1b  
 203 shows the average relative difference between  $T_1^0$  and  $\hat{T}_1^0$  as a function of geomagnetic colatitude.  
 204 We observe that the use of simplistic source models results in significant differences of the estimated  
 205 TFs, particularly for the imaginary part, which can potentially bias the inversion.

### 206 3.2 Data fit and recovered conductivity models

207 The transfer functions were individually inverted to determine the most probable set of conduc-  
 208 tivity profiles underneath 20 inland geomagnetic observatories (see Figure 2), for which synthetic  
 209 TFs can be computed with low computational cost using analytical solutions for radial 1-D Earth  
 210 models. Coastal and island geomagnetic observatories have been excluded from this analysis because  
 211 calculation of synthetic TFs for these locations require the use of 3-D solvers to account for ocean  
 212 induction effects [e.g., *Kuvshinov et al.*, 2002], making the use of Markov chain Monte Carlo methods  
 213 [e.g., *Mosegaard and Tarantola*, 1995] impracticable.

214 We succeed at explaining the observed daily and long-period EM variations for 13 geomagnetic  
 215 observatories (see Figures S5–S7), indicated in Figure 2 by red stars surrounded by black circles.  
 216 However, we find a cluster of 7 stations located in Europe (black circles in Figure S4) for which the  
 217 fit of daily transfer functions is unsatisfactory under the 1-D assumption (see Figures S6–S8). One  
 218 can speculate that this reflects: 1) the presence of anomalously shallow 3-D structure underneath  
 219 central Europe and the Mediterranean linked to the subduction and ponding of slabs in the MTZ as  
 220 suggested by seismic tomography [e.g., *Zhu et al.*, 2015; *Cottaar and Deuss*, 2016]; or 2) artifacts  
 221 due to the presence of noise (e.g., signals due to polar electrojet currents) that are not accounted for  
 222 in the presently used source parameterization.

223 Figure S4 illustrates the posterior probability distributions obtained when inverting daily and  
 224 long-period signals separately and jointly at a single station (Alice Spring in Australia). In agreement

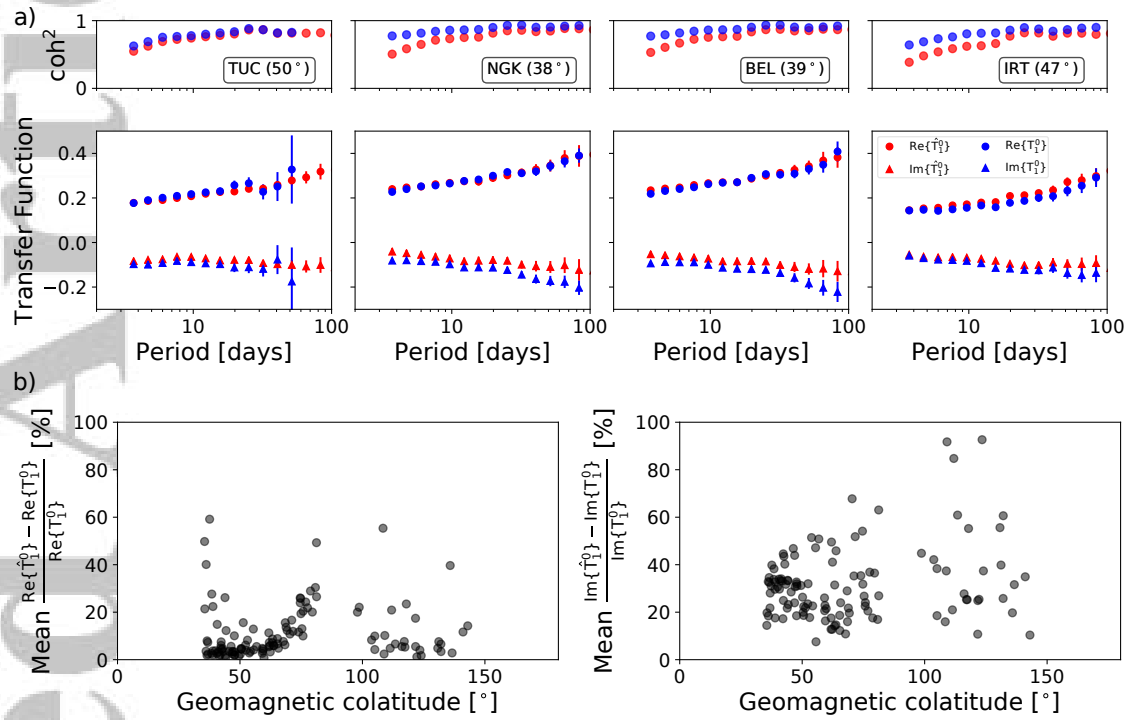


**Figure 1.** Example of experimental global-to-local transfer functions. a) Real (positive) and imaginary (negative) parts of the experimental global-to-local (blue) transfer functions  $T_1^0$  (bottom row) and squared coherencies  $\text{coh}^2$  (top row) estimated in this study for Boulder (BOU), Niemegek (NGK), Belsk (BEL), and Irkutsk (IRT) geomagnetic observatories. Geographic location of the geomagnetic observatories are shown in Figure 2. Error bars indicate uncertainties of the experimental transfer functions. For comparison, transfer functions  $\hat{T}_1^0$  obtained for a case when the source is described by the first zonal spherical harmonic are shown in red. b) Mean relative differences between the real (left) and imaginary (right) parts of  $T_1^0$  and  $\hat{T}_1^0$  as a function of geomagnetic colatitude.

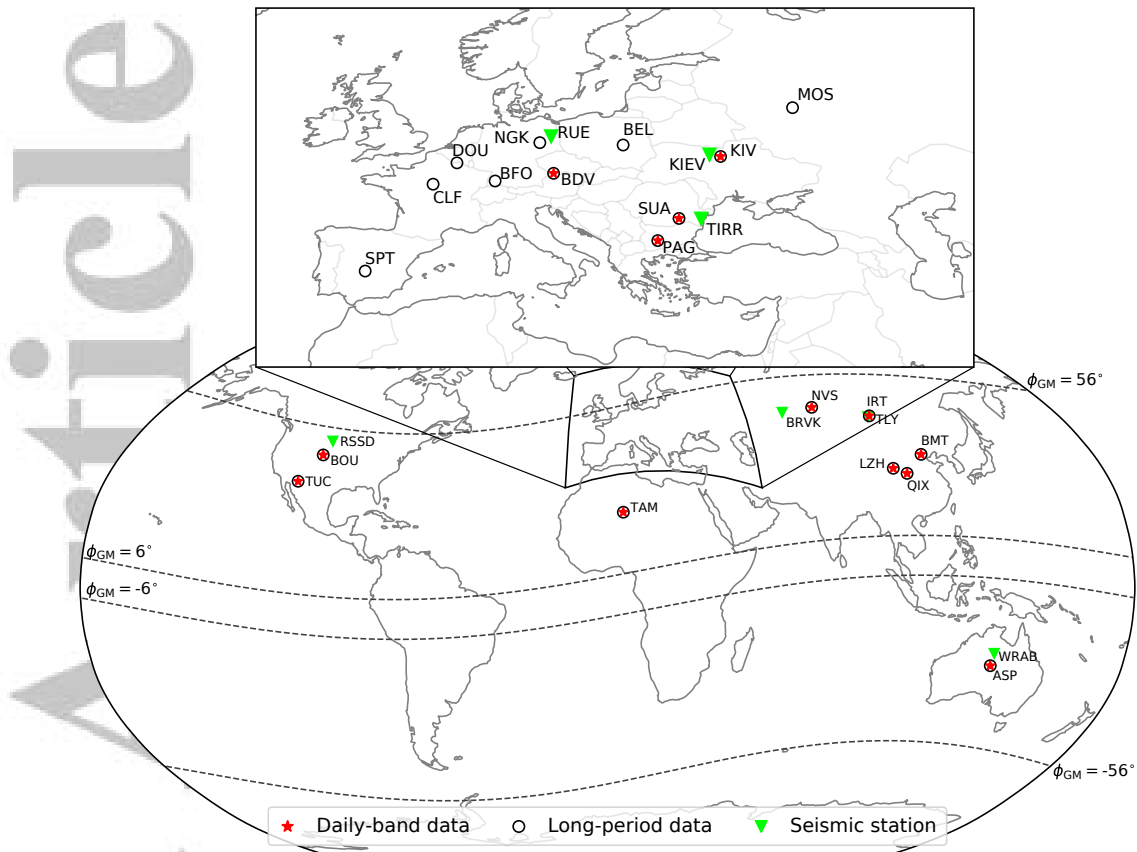


**Figure 2.** Geographic location of mid-latitude observatories used in this study between geomagnetic latitudes  $\phi_{GM} -56^\circ - -6^\circ$  and  $6^\circ - 56^\circ$ . Red stars and black circles denote stations at which the observed daily (6–24 hours) and long-period (3–85 days) transfer functions are successfully fitted in the inversion, respectively. Green triangles indicate seismic stations for which constraints on mantle temperature and composition were derived by *Munch et al.* [2020, in press] from analysis of short- and long-period seismic data. Station information is summarized in Table S1. Data fit for all stations is shown in Figures S5–S7.

225 with previous studies [e.g., *Munch et al.*, 2018], long-period signals best constrain the conductivity  
 226 structure in the depth range between 400 and 1400 km (see Figure S4b), while daily variations provide  
 227 information on the conductivity structure between 200 and 500 km depth (see Figure S4a) [e.g., *Koch*  
 228 *and Kuvshinov*, 2013]. The models obtained from the joint inversion of daily and long-period signals  
 229 (see Figure S4c) manage to resolve the conductivity structure in the upper mantle (200–400 km  
 230 depth), MTZ (400–660 km depth), and the uppermost lower mantle (660–1400 km depth).

### 231 3.3 Constraints on upper mantle and transition zone water content

232 We determined the range of water contents in olivine and wadsleyite that best explain the  
 233 inverted conductivity profiles between 200 and 1200 km depth. This was achieved by comparing the  
 234 inverted conductivity models with laboratory-based conductivity profiles (described in Section 2.3)  
 235 using an  $L_2$ -norm misfit function and the Metropolis algorithm. In particular, we focus on 8  
 236 geomagnetic observatories for which probability density functions of the mantle potential temperature  
 237 and composition (basalt fraction) derived from the inversion of short- and long-period seismic data  
 238 [Munch *et al.*, 2020, in press] recorded at a nearby station (indicated by triangles in Figure 2) are  
 239 available.

240 Figure 3 summarizes the conductivity models obtained from the joint inversion of long-period  
 241 and daily signals (black) and best-fitting laboratory-based conductivity profiles (green). Laboratory-  
 242 based conductivity profiles implicitly incorporate discontinuities across the major phase transitions  
 243 (olivine  $\rightarrow$  wadsleyite, wadsleyite  $\rightarrow$  ringwoodite, and ringwoodite  $\rightarrow$  bridgmanite+ferropericline),  
 244 whereas the conductivity models retrieved from the inversion of observed EM responses are smoother  
 245 down to depths of  $\sim 1000$  km. We find an overall agreement between the inverted conductivity models  
 246 and laboratory-based conductivity profiles particularly in the upper mantle and MTZ. However, we  
 247 observe that laboratory-based conductivity profiles are systematically more conductive in the lower  
 248 mantle (800–1200 km depth) than the conductivity models derived from the observed data. This  
 249 difference might reflect that 1) temperature estimates derived from the inversion of seismic data  
 250 might be biased towards higher temperatures; or 2) the laboratory-based conductivity databases  
 251 considered in this work tend to overestimate the electrical conductivity of lower mantle minerals.  
 252 Future work should aim at refining the laboratory-based mineral conductivity databases, particularly  
 253 for lower-mantle minerals, as the degree to which hydrogen affects the electrical conductivity of  
 254 lower mantle minerals remains uncertain. In this light, determining the influence of hydrogen on  
 255 electrical conductivity in the lower mantle minerals is critical to improve the current understanding  
 256 of the water distribution in the deep mantle and the circulation between the various reservoirs.

257 Figure 4 depicts inferences on water content in the upper mantle and MTZ minerals olivine  
 258 ( $C_w^{\text{ol}}$ ) and wadsleyite ( $C_w^{\text{wad}}$ ) obtained using the YK and KD databases. The former database generally  
 259 leads to a significantly more hydrated upper mantle and MTZ. As discussed by *Khan and Shankland*  
 260 [2012], this difference arises from the fact that the KD database tends to result in higher electrical  
 261 conductivities for a given water content. The use of the YK database results in anomalously high  
 262 water contents ( $C_w^{\text{ol}} \sim 0.3$  wt% and  $C_w^{\text{wad}} \sim 1.9$  wt%) underneath stations located in northern Asia (NVS

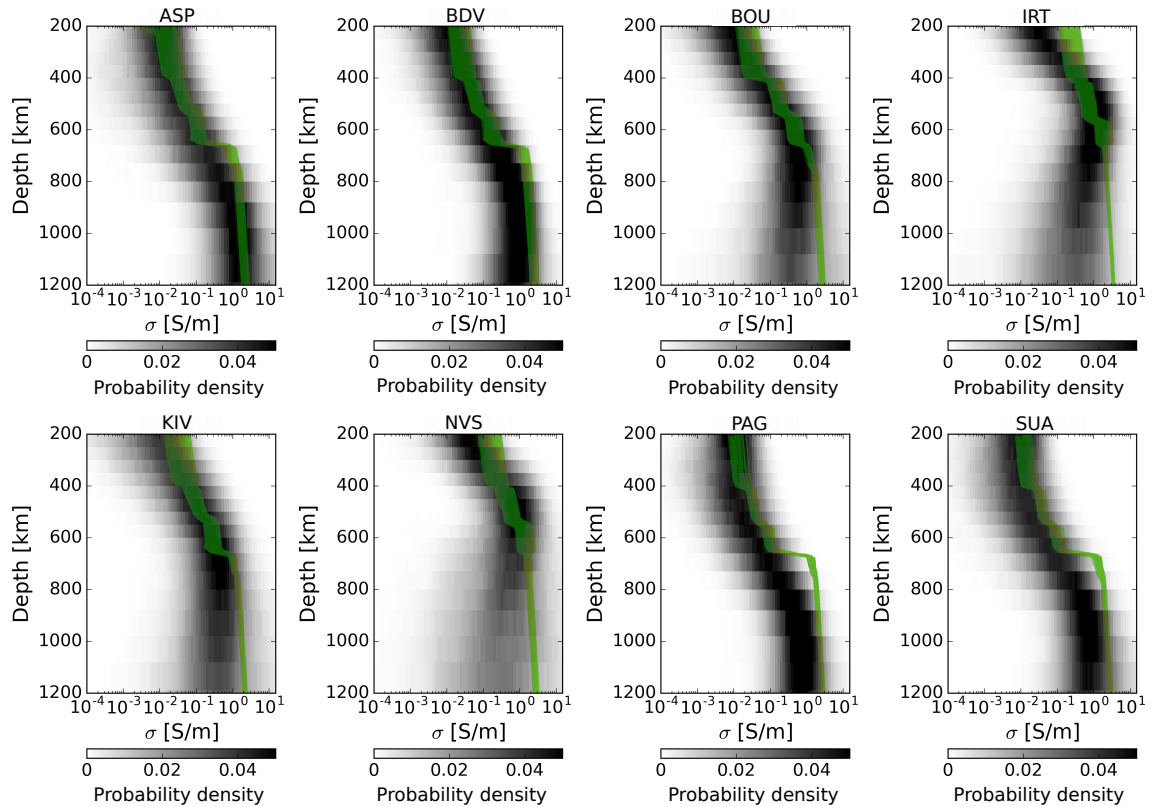


**Figure 3.** Posterior probability distributions of electrical conductivity ( $\sigma$ ) retrieved from the joint inversion of daily and long-period transfer functions (black) and best-fitting laboratory-based conductivity profiles (green) for the KD database. The geographic location of each geomagnetic observatory is shown in Figure 2 and station acronyms are defined in Table S1. Best-fitting laboratory-based conductivity profiles obtained using the YK database are shown in Figure S8.

and IRT). These estimates significantly exceed the experimentally-determined water storage capacity of mantle minerals [e.g., *Hirschmann et al.*, 2005; *Litasov et al.*, 2011], which would result in the accumulation of partial melt atop the MTZ [*Bercovici and Karato*, 2003]. However, no evidence for the existence of a melt layer (i.e., negative amplitudes on the receiver function waveforms due to a low shear-wave velocity anomaly) is observed in the seismic data and further analysis focuses on estimates derived with the KD database.

In agreement with previous studies [e.g., *Karato*, 2011; *Fullea et al.*, 2011; *Jones et al.*, 2012; *Khan and Shankland*, 2012], our results indicate a relatively dry upper mantle ( $C_w^{ol} < 0.02$  wt%) underneath all stations, whereas significant lateral variability in MTZ water content is observed. We find relatively low MTZ water contents ( $C_w^{wad} < 0.05$  wt%) in Australia (ASP) and Europe (BDV,

273 PAG, SUA, and KIV), whereas moderate ( $C_w^{\text{wad}} \sim 0.15$  wt%) and high water contents ( $C_w^{\text{wad}} \sim 0.3$  wt%)  
274 are required to explain the inverted conductivity profiles in Asia (IRT and NVS) and North America  
275 (BOU), respectively. A dry MTZ below Europe has already been suggested by *Utada et al.* [2009]  
276 from the joint analysis of seismic and electromagnetic models. In agreement with MTZ water  
277 contents experimentally determined by *Freitas et al.* [2017], our estimates suggest that the near-  
278 water saturated conditions implied by hydrous ringwoodite inclusions found in a natural diamond  
279 [*Pearson et al.*, 2014] are not representative of the whole MTZ.

#### 280 **4 Conclusions**

281 In this study, we combined EM responses in a wide period band to infer the electrical conductivity  
282 structure underneath a set of inland geomagnetic observatories, while accounting for complex spatial  
283 structure of the magnetospheric and ionospheric sources [*Püthe et al.*, 2015b]. We found that  
284 simplistic source models are likely to introduce significant errors in the estimated transfer functions  
285 and therefore, bias the inferred conductivity models. Furthermore, the incorporation of daily-band  
286 responses (6–24 h) into the inversion leads to improved model resolution, especially in the upper  
287 mantle and transition zone.

288 The retrieved conductivity models were subsequently interpreted in terms of variations in  
289 upper mantle (olivine) and transition zone (wadsleyite) water content by combining mineral phase  
290 equilibria calculations, laboratory-based electrical conductivity measurements, and estimates on  
291 mantle temperature and major element chemistry derived independently from the inversion of short-  
292 and long-period seismic data. We find the existence of a relatively dry transition zone beneath  
293 Europe ( $C_w^{\text{wad}} < 0.05$  wt%) and a water-enriched ( $C_w^{\text{wad}} \sim 0.3$  wt%) transition zone underneath North  
294 America and northern Asia. These findings suggest that the near-water saturated conditions hinted  
295 at by hydrous ringwoodite inclusions found in a natural diamond [*Pearson et al.*, 2014] are not likely  
296 to be representative of the entire MTZ.

297 The methodology presented here provides quantitative constraints on water content in the upper  
298 mantle and transition zone. To move beyond the current results and improve our understanding of  
299 the water distribution in the deep mantle and mantle water circulation, future work should aim at:  
300 1) extending the geographical distribution of geomagnetic observatories to include data from coastal  
301 and island; and 2) inverting EM and seismic data jointly by means of an integrated approach [e.g.,  
302 *Khan*, 2016]. The former demands the use of 3-D EM solvers to account for the ocean induction  
303 effect [e.g., *Kuvshinov et al.*, 2002], which makes the implementation of Markov chain Monte

304 Carlo methods impracticable. The latter requires a refinement of the laboratory-based electrical  
305 conductivity databases to lower-mantle minerals, and the extension of the thermodynamic database  
306 employed for mineral phase equilibria calculations to account for effects related to oxygen fugacity,  
307 water content, and melt.

Accepted Article

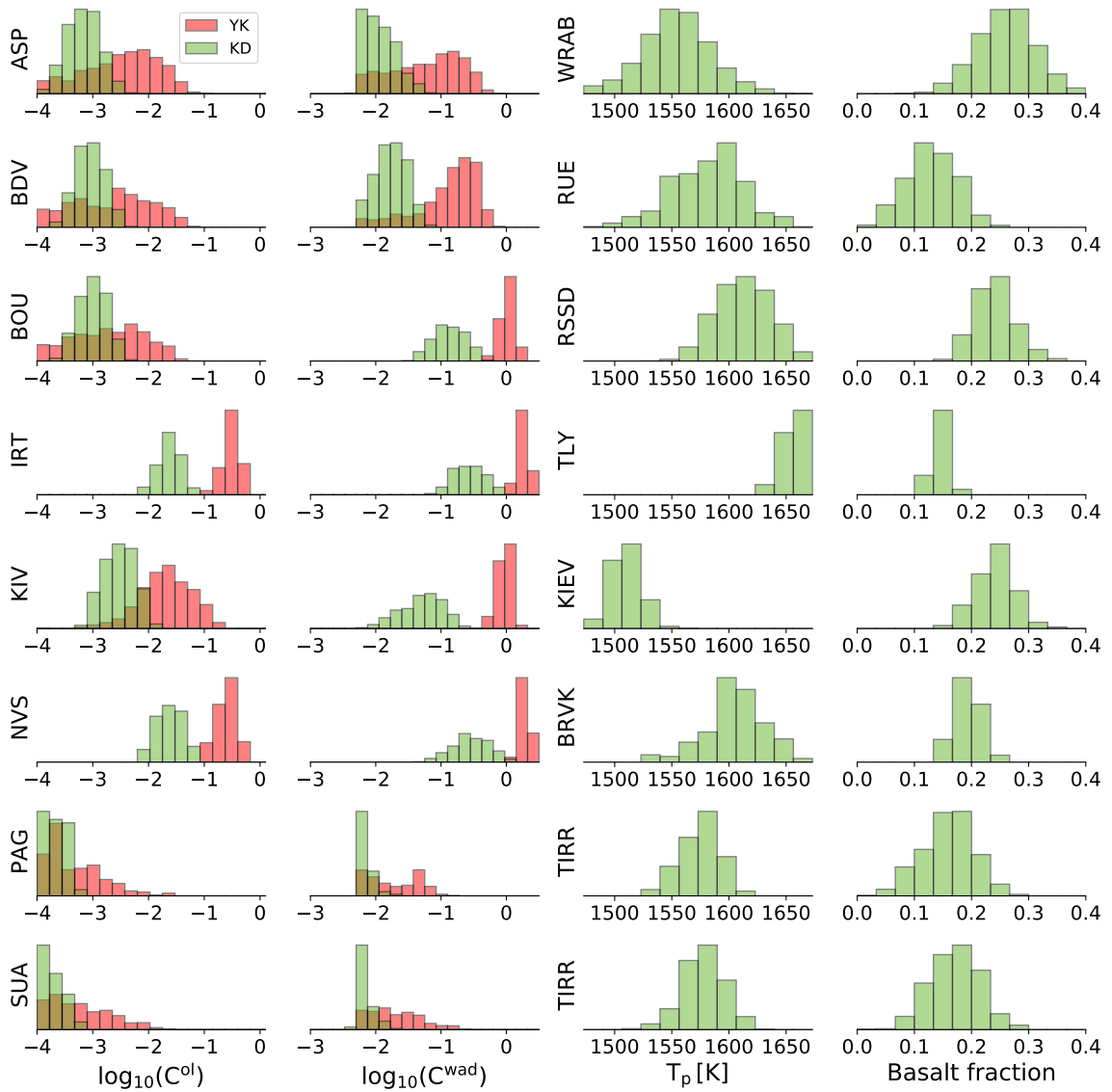


**Figure 4.** Sampled water content in (a) olivine and (b) wadsleyite retrieved using the Yoshino-Katsura (YK) and Karato-Dai (KD) electrical conductivity databases. Water contents are given in terms of  $C^x = C_w^x/C_w^0$ , where  $x$  denotes either of the minerals olivine and wadsleyite,  $C_w^x$  is in wt%, and  $C_w^0 = 1$  wt%. Constraints on the probability distribution of (c) mantle potential temperature ( $T_p$ ) and (d) composition (basalt fraction) were obtained from the inversion of P-to-s receiver functions and Rayleigh wave phase velocities [Munch *et al.*, 2020, in press]. Station acronyms are defined in Table S1 and geographic locations are depicted in Figure 2.

### Acknowledgments

We are grateful to two anonymous reviewers for their constructive comments, which helped improve the manuscript. F.D.M. was supported by a grant from the Swiss National Science Foundation



311 (Project No. 159907). A.G. and A.V.K. were supported by ESA through the Swarm DISC project.  
 312 M.G. was supported by ETH Grant No. ETH-3215-2. The authors would also like to acknowledge  
 313 the British Geological Survey (BGS), WDC Geomagnetism (Edinburgh), INTERMAGNET, and  
 314 the many Institutes around the World that operate magnetic observatories. Time series of geomag-  
 315 netic field components used in this study are available on [ftp://ftp.nerc-murchison.ac.uk/  
 geomag/Swarm/AUX\\_OBS/hour](ftp://ftp.nerc-murchison.ac.uk/geomag/Swarm/AUX_OBS/hour). Long-period transfer functions and main inversion results (con-  
 317 ductivity profiles, water content, basalt fraction, and mantle potential temperature estimates) for each  
 318 stations are available on <https://doi.org/10.3929/ethz-b-000405622>.

### 319 **Appendix A: Estimation of magnetospheric source coefficients**

320 Maxwell's equations describe the spatio-temporal behavior of electromagnetic fields and can  
 321 be formulated in frequency domain as

$$\frac{1}{\mu_0} \nabla \times \mathbf{B}(\mathbf{r}, \omega) = \sigma(\mathbf{r})\mathbf{E}(\mathbf{r}, \omega) + \mathbf{j}^{\text{ext}}(\mathbf{r}, \omega), \quad (4)$$

$$\nabla \times \mathbf{E}(\mathbf{r}, \omega) = i\omega\mathbf{B}(\mathbf{r}, \omega), \quad (5)$$

322 where  $\mathbf{B}$  and  $\mathbf{E}$  represent the complex Fourier transforms of magnetic flux density and electric field at  
 323 a location  $\mathbf{r} = (r, \vartheta, \varphi)$ . The distance from the Earth's center is denoted by  $r$ ,  $\vartheta$  is the colatitude, and  
 324  $\varphi$  is the longitude. Furthermore,  $\mathbf{j}^{\text{ext}}(\mathbf{r}, \omega)$  is the complex Fourier transform of an impressed source  
 325 current density,  $\sigma(\mathbf{r})$  represents the electrical conductivity distribution in the media,  $\omega$  is the angular  
 326 frequency, and  $\mu_0$  is the magnetic permeability of free space. Given that deep electromagnetic (EM)  
 327 studies consider induction due to natural current systems which vary on time scales between a few  
 328 hours and a few months, displacement currents are here neglected.

329 Above the conducting Earth and below the region enclosed by the current  $\mathbf{j}^{\text{ext}}$ , Eq. (4) reduces  
 330 to  $\nabla \times \mathbf{B} = 0$ , thus  $\mathbf{B}$  is a potential field that can be described as a gradient of a scalar potential  $V$

$$\mathbf{B} = -\nabla V. \quad (6)$$

Since  $\nabla \cdot \mathbf{B} = 0$ , then  $V$  satisfies Laplace's equation ( $\nabla^2 V = 0$ ) and hence, can be decomposed into  
 external and internal parts such that  $V = V^{\text{ext}} + V^{\text{int}}$ , where

$$V^{\text{ext}} = a \sum_{n=1}^{N_e} \sum_{m=-n}^n \varepsilon_n^m(\omega) \left(\frac{r}{a}\right)^n Y_n^m(\vartheta, \varphi), \quad (7)$$

$$V^{\text{int}} = a \sum_{k=1}^{N_i} \sum_{l=-k}^k \iota_k^l(\omega) \left(\frac{r}{a}\right)^{-(k+1)} Y_k^l(\vartheta, \varphi), \quad (8)$$

331 where  $\varepsilon_n^m(\omega)$  and  $\iota_k^l(\omega)$  are the spherical harmonic expansion (SHE) coefficients of the external  
 332 (inducing) and internal (induced) parts of the potential,  $N_\varepsilon$  and  $N_\iota$  are the maximum (cut-off)  
 333 degrees for external and internal coefficients, respectively, and  $Y_n^m$  is the spherical harmonic of  
 334 degree  $n$  and order  $m$

$$Y_n^m(\vartheta, \varphi) = P_n^{|m|}(\cos \vartheta) e^{im\varphi}, \quad (9)$$

335 where  $P_n^{|m|}(\cos \vartheta)$  corresponds to the Schmidt quasi-normalized associated Legendre function of  
 336 degree  $n$  and order  $|m|$ . Note that in Eqs. (7) and (8), we use different indices for external and internal  
 337 coefficients to account for the 3-D conductivity distribution. In a 1-D Earth (in which conductivity  
 338 is only a function of depth), every external coefficient only induces one internal coefficient of the  
 339 same degree and order. They are linearly related by the (scalar) Q-response, which is defined as

$$\iota_n^m(\omega) = Q_n(\omega) \varepsilon_n^m(\omega). \quad (10)$$

340 Note that in 1-D case,  $Q_n$  is independent of the order  $m$  [e.g., *Bailey, 1969*] and  $N_\varepsilon = N_\iota$ . In a 3-D  
 341 Earth, however, every external coefficient  $\varepsilon_n^m$  induces a whole series of internal coefficients  $\iota_k^l$  such  
 342 that we can write

$$\iota_k^l(\omega) = \sum_{n=1}^{N_\varepsilon} \sum_{m=-n}^n Q_{kn}^{lm}(\omega) \varepsilon_n^m(\omega), \quad (11)$$

where the  $Q_{kn}^{lm}$  form a 2-D array of transfer functions we refer to as Q-matrix. The diagonal elements  
 of this matrix mostly describe the bulk conductivity and, in case of a layered (1-D) Earth, they  
 are equivalent to the scalar Q-responses. The off-diagonal elements describe a transfer of energy to  
 coefficients of different degree and order, which only occurs if the subsurface has a 3-D structure. Note  
 that our a priori 3-D Earth's model consists of a mantle with 1-D conductivity distribution overlaid  
 by a surface layer of known laterally-variable conductance; the latter approximates nonuniform  
 distribution of oceans and continents. Our numerical experiments shows that the diagonal elements  
 of corresponding Q-matrix are dominant for the considered period range (3–85 days). Therefore,  
 exploiting Eqs. (6)-(8) and (11), the magnetic field on the surface of the Earth,  $\mathbf{r}_a = (a, \vartheta, \varphi)$ , can  
 be written as

$$\mathbf{B}_r(\mathbf{r}_a, \omega) = - \sum_{n=1}^{N_\varepsilon} \sum_{m=-n}^n \varepsilon_n^m(\omega) [n - (n+1) Q_{nn}^{mm}(\omega)] Y_n^m(\vartheta, \varphi), \quad (12)$$

$$\mathbf{B}_\tau(\mathbf{r}_a, \omega) = - \sum_{n=1}^{N_\varepsilon} \sum_{m=-n}^n \varepsilon_n^m(\omega) [1 + Q_{nn}^{mm}(\omega)] \nabla_\perp Y_n^m(\vartheta, \varphi), \quad (13)$$

343 where subscript  $\tau$  denotes the tangential part of  $\mathbf{B}$  and  $\nabla_\perp$  is the surface gradient. With the following  
 344 denotation

$$v_n^m(\omega) = \varepsilon_n^m(\omega) [1 + Q_{nn}^{mm}(\omega)], \quad (14)$$

time domain equivalent of Eq. (13) reads

$$\mathbf{B}_r(\mathbf{r}_a, t) = - \sum_{n=1}^{N_\varepsilon} \sum_{m=-n}^n v_n^m(t) \nabla_\perp Y_n^m(\vartheta, \varphi). \quad (15)$$

In this study, we estimated external source coefficients  $\epsilon_n^m(t)$  following the procedure proposed by *Püthe et al.* [2015b]. This procedure can be summarized as follows:

- (1) Collection of hourly-mean time series of geomagnetic field components from mid-latitude permanent observatories (see Figure S1) from the British Geological Survey database [*Macmillan and Olsen, 2013*].
- (2) Removal of the main field and its secular variations using the CHAOS model [*Olsen et al., 2006*].
- (3) Detrend each magnetic field component using cubic B-splines.
- (4) Rotation of the horizontal magnetic field components from geographic to geomagnetic coordinates using geomagnetic north pole coordinates for the year 2010.
- (5) Estimation of  $v_n^m$  for each time instant  $t$  from the tangential components of the observed magnetic field in geomagnetic coordinates using Eq. (15) and a Huber-weighted robust least-squares method [e.g., *Aster et al., 2005*]. Weights are meant to counteract potential biases introduced by cluster of stations (e.g., the high concentrations of observatories in the Northern hemisphere). At each time instant  $t$ , we triangulate the spatial distribution of observatories (via calculating the convex hull). Weights are then estimated as the surface area of the spherical triangle that has a given observatory as its center.
- (6) Separation of internal and external contributions as follows:
  - A. Transformation of the unseparated coefficients  $v_n^m(t)$  into frequency domain.
  - B. Computation of radial magnetic field  $B_{n,r}^m(\mathbf{r}_a, \omega)$  induced by unit amplitude spherical harmonic sources ( $\epsilon_n^m = 1$ ) in frequency domain using a numerical solver based on integral equation approach [*Kuvshinov, 2008*]. As mentioned above, computations are performed in a priori 3-D Earth's model consisting of a mantle with 1-D conductivity distribution overlaid by a surface layer of laterally-variable conductance.
  - C. Calculation of  $Q_{nn}^{mm}(\omega)$  from the computed  $B_{n,r}^m(\mathbf{r}_a, \omega)$  as [*Püthe and Kuvshinov, 2014*]

$$Q_{nn}^{mm}(\omega) = \frac{1}{(n+1) \|Y_n^m\|^2} \int_{\Omega} [B_{n,r}^m(\mathbf{r}_a, \omega) - B_{n,r}^{m,ext}(\mathbf{r}_a)] \hat{Y}_n^m(\vartheta, \varphi) ds. \quad (16)$$

370 Here  $\hat{Y}_n^m$  denotes complex conjugation  $Y_n^m$ ,  $\Omega$  is the complete solid angle,  $ds = \sin \vartheta d\vartheta d\varphi$ ,  
 371 and  $\|Y_n^m\|^2$  is the squared norm of the spherical harmonic  $Y_n^m$ , and  $B_{n,r}^{m,ext}$  is the external  
 372 part of radial magnetic field, i.e.

$$B_{n,r}^{m,ext}(\mathbf{r}_a) = -nY_n^m(\vartheta, \varphi). \quad (17)$$

373 Substituting Eq. (17) into Eq. (16) we have

$$Q_{nn}^{mm}(\omega) = \frac{1}{(n+1)\|Y_n^m\|^2} \int_{\Omega} B_{n,r}^m(\mathbf{r}_a, \omega) \hat{Y}_n^m(\vartheta, \varphi) ds + \frac{n}{n+1}. \quad (18)$$

374 D. Separation of internal and external contributions using Eq. (14)

$$375 \epsilon_n^m(\omega) = v_n^m(\omega) / [1 + Q_{nn}^{mm}(\omega)].$$

376 E. Transformation of the external coefficients  $\epsilon_n^m(\omega)$  into time domain.

## 377 References

- 378 Aster, R., B. Borchers, and C. Thurber (2005), *Parameter estimation and inverse problems*: Elsevier  
 379 academic.
- 380 Bahr, K., N. Olsen, and T. J. Shankland (1993), On the combination of the magnetotelluric and the  
 381 geomagnetic depth sounding method for resolving an electrical conductivity increase at 400 km  
 382 depth, *Geophysical research letters*, *20*(24), 2937–2940.
- 383 Bailey, R. (1969), Inversion of the geomagnetic induction problem, *Proc. R. Soc. Lond.*, *315*, 185–  
 384 194.
- 385 Balasis, G., and G. D. Egbert (2006), Empirical orthogonal function analysis of magnetic observa-  
 386 tory data: Further evidence for non-axisymmetric magnetospheric sources for satellite induction  
 387 studies, *Geophysical research letters*, *33*(11).
- 388 Banks, R. (1969), Geomagnetic variations and the electrical conductivity of the upper mantle,  
 389 *Geophysical Journal International*, *17*(5), 457–487.
- 390 Bercovici, D., and S.-i. Karato (2003), Whole-mantle convection and the transition-zone water filter,  
 391 *Nature*, *425*(6953), 39–44.
- 392 Bolfan-Casanova, N. (2005), Water in the Earth's mantle, *Mineralogical Magazine*, *69*(3), 229–257.
- 393 Bolfan-Casanova, N., C. A. Mccammon, and S. J. Mackwell (2006), Water in transition zone and  
 394 lower mantle minerals, *GEOPHYSICAL MONOGRAPH-AMERICAN GEOPHYSICAL UNION*,  
 395 *168*, 57.
- 396 Connolly, J. (2009), The geodynamic equation of state: what and how, *Geochemistry, Geophysics,*  
 397 *Geosystems*, *10*(10).

- 398 Cottaar, S., and A. Deuss (2016), Large-scale mantle discontinuity topography beneath Europe:  
399 Signature of akimotoite in subducting slabs, *Journal of Geophysical Research: Solid Earth*,  
400 *121*(1), 279–292.
- 401 Daglis, I., and J. Kozyra (2002), Outstanding issues of ring current dynamics, *Journal of atmospheric  
402 and solar-terrestrial physics*, *64*(2), 253–264.
- 403 Egbert, G. D., and J. R. Booker (1992), Very long period magnetotellurics at Tucson observatory:  
404 implications for mantle conductivity, *Journal of Geophysical Research: Solid Earth*, *97*(B11),  
405 15,099–15,112.
- 406 Ferot, A., and N. Bolfan-Casanova (2012), Water storage capacity in olivine and pyroxene to 14GPa:  
407 Implications for the water content of the Earth's upper mantle and nature of seismic discontinuities,  
408 *Earth and Planetary Science Letters*, *349*, 218–230.
- 409 Finlay, C., V. Lesur, E. Thébault, F. Vervelidou, A. Morschhauser, and R. Shore (2017), Challenges  
410 handling magnetospheric and ionospheric signals in internal geomagnetic field modelling.
- 411 Freitas, D., G. Manthilake, F. Schiavi, J. Chantel, N. Bolfan-Casanova, M. Bouhifd, and D. Andrault  
412 (2017), Experimental evidence supporting a global melt layer at the base of the Earth's upper  
413 mantle, *Nature communications*, *8*(1), 2186.
- 414 Fulla, J., M. Muller, and A. Jones (2011), Electrical conductivity of continental lithospheric mantle  
415 from integrated geophysical and petrological modeling: Application to the Kaapvaal Craton and  
416 Rehoboth Terrane, southern Africa, *Journal of Geophysical Research: Solid Earth*, *116*(B10).
- 417 Grayver, A., F. Munch, A. Kuvshinov, A. Khan, T. Sabaka, and L. Tøffner-Clausen (2017), Joint  
418 inversion of satellite-detected tidal and magnetospheric signals constrains electrical conductivity  
419 and water content of the upper mantle and transition zone, *Geophysical Research Letters*.
- 420 Grayver, A. V., and A. V. Kuvshinov (2016), Exploring equivalence domain in nonlinear inverse  
421 problems using Covariance Matrix Adaption Evolution Strategy (CMAES) and random sampling,  
422 *Geophysical Journal International*, *205*(2), 971–987.
- 423 Guzavina, M., A. Grayver, and A. Kuvshinov (2019), Probing upper mantle electrical conductiv-  
424 ity with daily magnetic variations using global-to-local transfer functions, *Geophysical Journal  
425 International*, *219*(3), 2125–2147.
- 426 Hansen, N., and A. Ostermeier (2001), Completely derandomized self-adaptation in evolution strate-  
427 gies, *Evolutionary computation*, *9*(2), 159–195.
- 428 Hansen, P. C. (1999), The L-curve and its use in the numerical treatment of inverse problems.
- 429 Hastings, W. K. (1970), Monte Carlo sampling methods using Markov chains and their applications,  
430 *Biometrika*, *57*(1), 97–109.

- 431 Hirschmann, M. M. (2006), Water, melting, and the deep Earth H<sub>2</sub>O cycle, *Annu. Rev. Earth Planet.*  
432 *Sci.*, *34*, 629–653.
- 433 Hirschmann, M. M., C. Aubaud, and A. C. Withers (2005), Storage capacity of H<sub>2</sub>O in nominally  
434 anhydrous minerals in the upper mantle, *Earth and Planetary Science Letters*, *236*(1), 167–181.
- 435 Inoue, T., T. Wada, R. Sasaki, and H. Yurimoto (2010), Water partitioning in the Earth's mantle,  
436 *Physics of the Earth and Planetary Interiors*, *183*(1), 245–251.
- 437 Jones, A. G., J. Fulla, R. L. Evans, and M. R. Muller (2012), Water in cratonic lithosphere:  
438 Calibrating laboratory-determined models of electrical conductivity of mantle minerals using  
439 geophysical and petrological observations, *Geochemistry, Geophysics, Geosystems*, *13*(6).
- 440 Karato, S.-i. (2011), Water distribution across the mantle transition zone and its implications for  
441 global material circulation, *Earth and Planetary Science Letters*, *301*(3), 413–423.
- 442 Katsura, T., and T. Yoshino (2015), Heterogeneity of electrical conductivity in the oceanic upper  
443 mantle, in *The Earth's Heterogeneous Mantle*, pp. 173–204, Springer.
- 444 Kelbert, A., A. Schultz, and G. Egbert (2009), Global electromagnetic induction constraints on  
445 transition-zone water content variations, *Nature*, *460*(7258), 1003–1006.
- 446 Khan, A. (2016), On Earth's mantle constitution and structure from joint analysis of geophysical and  
447 laboratory-based data: An example, *Surveys in Geophysics*, *37*(1), 149–189.
- 448 Khan, A., and T. Shankland (2012), A geophysical perspective on mantle water content and melting:  
449 Inverting electromagnetic sounding data using laboratory-based electrical conductivity profiles,  
450 *Earth and Planetary Science Letters*, *317*, 27–43.
- 451 Koch, S., and A. Kuvshinov (2013), Global 3-D EM inversion of Sq variations based on simultaneous  
452 source and conductivity determination: concept validation and resolution studies, *Geophysical*  
453 *Journal International*, *195*(1), 98–116.
- 454 Koyama, T., H. Shimizu, H. Utada, M. Ichiki, E. Ohtani, and R. Hae (2006), Water content in the  
455 mantle transition zone beneath the north pacific derived from the electrical conductivity anomaly,  
456 *Earth's Deep Water Cycle*, pp. 171–179.
- 457 Koyama, T., A. Khan, and A. Kuvshinov (2014), Three-dimensional electrical conductivity structure  
458 beneath Australia from inversion of geomagnetic observatory data: evidence for lateral variations  
459 in transition-zone temperature, water content and melt, *Geophysical Journal International*, *196*(3),  
460 1330.
- 461 Kuvshinov, A. (2008), 3-D global induction in the oceans and solid Earth: recent progress in  
462 modeling magnetic and electric fields from sources of magnetospheric, ionospheric and oceanic  
463 origin, *Surveys in geophysics*, *29*(2), 139–186.

- 464 Kuvshinov, A. V., N. Olsen, D. B. Avdeev, and O. V. Pankratov (2002), Electromagnetic induction  
465 in the oceans and the anomalous behaviour of coastal C-responses for periods up to 20 days,  
466 *Geophysical research letters*, 29(12).
- 467 Litasov, K. D., A. Shatskiy, E. Ohtani, and T. Katsura (2011), Systematic study of hydrogen incor-  
468 poration into Fe-free wadsleyite, *Physics and Chemistry of Minerals*, 38(1), 75–84.
- 469 Macmillan, S., and N. Olsen (2013), Observatory data and the Swarm mission, *Earth, Planets and*  
470 *Space*, 65(11), 1355–1362.
- 471 McKenzie, D., and M. Bickle (1988), The volume and composition of melt generated by extension  
472 of the lithosphere, *Journal of petrology*, 29(3), 625–679.
- 473 Metropolis, N., A. W. Rosenbluth, M. N. Rosenbluth, A. H. Teller, and E. Teller (1953), Equation of  
474 state calculations by fast computing machines, *The journal of chemical physics*, 21(6), 1087–1092.
- 475 Mookherjee, M., and S.-i. Karato (2010), Solubility of water in pyrope-rich garnet at high pressures  
476 and temperature, *Geophysical Research Letters*, 37(3).
- 477 Mosegaard, K., and A. Tarantola (1995), Monte Carlo sampling of solutions to inverse problems,  
478 *Journal of Geophysical Research: Solid Earth*, 100(B7), 12,431–12,447.
- 479 Munch, F., A. Grayver, A. Kuvshinov, and A. Khan (2018), Stochastic inversion of geomagnetic  
480 observatory data including rigorous treatment of the ocean induction effect with implications  
481 for transition zone water content and thermal structure, *Journal of Geophysical Research: Solid*  
482 *Earth*, 123(1), 31–51.
- 483 Munch, F., A. Khan, B. Tauzin, M. van Driel, and D. Giardini (2020, in press), Seismological  
484 evidence for the existence of thermo-chemical heterogeneity in Earth’s continental mantle, *Earth*  
485 *and Planetary Science Letters*.
- 486 Ohtani, E., K. Litasov, T. Hosoya, T. Kubo, and T. Kondo (2004), Water transport into the deep  
487 mantle and formation of a hydrous transition zone, *Physics of the Earth and Planetary Interiors*,  
488 143, 255–269.
- 489 Olsen, N. (1998), The electrical conductivity of the mantle beneath Europe derived from C-responses  
490 from 3 to 720 hr, *Geophysical Journal International*, 133(2), 298–308.
- 491 Olsen, N., and A. Kuvshinov (2004), Modeling the ocean effect of geomagnetic storms, *Earth,*  
492 *planets and space*, 56(5), 525–530.
- 493 Olsen, N., and C. Stolle (2017), Magnetic signatures of ionospheric and magnetospheric current  
494 systems during geomagnetic quiet conditions—an overview, *Space Science Reviews*, 206(1-4),  
495 5–25.

- 496 Olsen, N., H. Lühr, T. J. Sabaka, M. Manda, M. Rother, L. Tøffner-Clausen, and S. Choi (2006),  
497 CHAOS— A model of the Earth's magnetic field derived from CHAMP, Ørsted, and SAC-C  
498 magnetic satellite data, *Geophysical Journal International*, 166(1), 67–75.
- 499 Pearson, D., F. Brenker, F. Nestola, J. McNeill, L. Nasdala, M. Hutchison, S. Matveev, K. Mather,  
500 G. Silversmit, S. Schmitz, et al. (2014), Hydrous mantle transition zone indicated by ringwoodite  
501 included within diamond, *Nature*, 507(7491), 221.
- 502 Peslier, A. H., and M. Bizimis (2015), Water in Hawaiian peridotite minerals: A case for a dry  
503 metasomatized oceanic mantle lithosphere, *Geochemistry, Geophysics, Geosystems*, 16(4), 1211–  
504 1232.
- 505 Peslier, A. H., A. B. Woodland, D. R. Bell, and M. Lazarov (2010), Olivine water contents in the  
506 continental lithosphere and the longevity of cratons, *Nature*, 467(7311), 78.
- 507 Püthe, C., and A. Kuvshinov (2014), Mapping 3-D mantle electrical conductivity from space: a new  
508 3-D inversion scheme based on analysis of matrix Q-responses, *Geophysical Journal International*,  
509 197(2), 768–784.
- 510 Püthe, C., A. Kuvshinov, A. Khan, and N. Olsen (2015a), A new model of Earth's radial conductivity  
511 structure derived from over 10 yr of satellite and observatory magnetic data, *Geophysical Journal  
512 International*, 203(3), 1864–1872.
- 513 Püthe, C., A. Kuvshinov, and N. Olsen (2015b), Handling complex source structures in global EM  
514 induction studies: from C-responses to new arrays of transfer functions, *Geophysical Journal  
515 International*, 201(1), 318–328.
- 516 Semenov, A., and A. Kuvshinov (2012), Global 3-D imaging of mantle conductivity based on inver-  
517 sion of observatory C-responses—II. Data analysis and results, *Geophysical Journal International*,  
518 191(3), 965–992.
- 519 Shimizu, H., H. Utada, K. Baba, T. Koyama, M. Obayashi, and Y. Fukao (2010), Three-dimensional  
520 imaging of electrical conductivity in the mantle transition zone beneath the North Pacific Ocean  
521 by a semi-global induction study, *Physics of the Earth and Planetary Interiors*, 183(1), 252–269.
- 522 Stixrude, L., and C. Lithgow-Bertelloni (2005), Thermodynamics of mantle minerals-I. physical  
523 properties, *Geophysical Journal International*, 162(2), 610–632.
- 524 Stixrude, L., and C. Lithgow-Bertelloni (2011), Thermodynamics of mantle minerals-II. Phase  
525 equilibria, *Geophysical Journal International*, 184(3), 1180–1213.
- 526 Sun, J., A. Kelbert, and G. Egbert (2015), Ionospheric current source modeling and global geomag-  
527 netic induction using ground geomagnetic observatory data, *Journal of Geophysical Research:  
528 Solid Earth*, 120(10), 6771–6796.



529 Tarantola, A., and B. Valette (1982), Generalized nonlinear inverse problems solved using the least  
530 squares criterion, *Reviews of Geophysics*, 20(2), 219–232.

531 Utada, H., T. Koyama, M. Obayashi, and Y. Fukao (2009), A joint interpretation of electromagnetic  
532 and seismic tomography models suggests the mantle transition zone below Europe is dry, *Earth  
533 and Planetary Science Letters*, 281(3), 249–257.

534 Yamazaki, Y., and A. Maute (2017), Sq and EEJ—A review on the daily variation of the geomagnetic  
535 field caused by ionospheric dynamo currents, *Space Science Reviews*, 206(1-4), 299–405.

536 Zhu, H., E. Bozdağ, and J. Tromp (2015), Seismic structure of the European upper mantle based on  
537 adjoint tomography, *Geophysical Journal International*, 201(1), 18–52.

Accepted Article